







The Pitch-angle Distributions of Suprathermal Ions near an Interplanetary Shock

Liu Yang^{1,2} , Lars Berger², Robert F. Wimmer-Schweingruber^{2,3} , Linghua Wang¹ , Jia Yu², Antoinette B. Galvin⁴, and Eberhard Möbius⁴ 

¹ School of Earth and Space Sciences, Peking University, Beijing, 100871, People's Republic of China; yangliu@pku.edu.cn

² Institute of Experimental and Applied Physics, University of Kiel, Leibnizstrasse 11, D-24118 Kiel, Germany

³ National Space Science Center, Beijing, 100190, People's Republic of China

⁴ Institute for the Study of Earth, Oceans and Space, University of New Hampshire, SSC Morse Hall, Durham, NH 03824, USA

Received 2019 October 8; revised 2019 December 16; accepted 2019 December 17; published 2020 January 13

Abstract

We present a case study of the pitch-angle distributions (PADs) of suprathermal H^+ , He^{2+} at $\sim 10\text{--}40$ keV/nuc and He^+ at $\sim 8\text{--}20$ keV/nuc near a reverse shock of a stream interaction region observed by the Plasma and Suprathermal Ion Composition instrument on board the *Solar Terrestrial Relations Observatory Ahead* spacecraft on 2008 March 9. We find that in both the downstream and upstream region close to the shock, the shocked particles of all three species appear to have a power-law-like spectrum at these suprathermal energies. The PADs of these three species show very similar behavior: in the downstream region, the phase space density appears to be significantly higher in the direction perpendicular to the interplanetary magnetic field (IMF) than in the parallel direction, along which particles accelerated at the shock front are supposed to escape into the downstream region. In the upstream region, the PADs of all three species show a clear beam in the direction antiparallel to the IMF due to the escaping particles from the shock into the upstream region. In addition, we find that suprathermal He^+ shows a signature of bidirectional beams in the upstream region very close to the shock. These results suggest that H^+ , He^{2+} at $\sim 10\text{--}40$ keV/nuc and He^+ at $\sim 8\text{--}20$ keV/nuc could be accelerated similarly at interplanetary shocks and that shock drift acceleration likely plays an important role in the in situ acceleration of low-energy suprathermal ions.

Unified Astronomy Thesaurus concepts: [Interplanetary particle acceleration \(826\)](#); [Interplanetary shocks \(829\)](#); [Solar wind \(1534\)](#); [Corotating streams \(314\)](#)

1. Introduction

Interplanetary collisionless shocks are capable of accelerating charged particles up to tens or even hundreds of MeV (e.g., Bryant et al. 1962; Asbridge et al. 1968; Kennel et al. 1984; Tsurutani & Lin 1985; Dresing et al. 2016). It is frequently observed that energetic particle fluxes are enhanced at the shock as well as in its downstream region, and they show a power-law energy spectrum (e.g., Tsurutani et al. 1982; Ho et al. 2003; Fisk & Gloeckler 2012; Giacalone 2012). The theory of diffusive shock acceleration predicts such a power-law energy spectrum downstream of the shock and is thus widely accepted as the source of interplanetary energetic particles (e.g., Kallenrode 2013; Desai & Giacalone 2016; Qin et al. 2018). The theory of diffusive shock acceleration incorporates two major acceleration mechanisms: first-order Fermi acceleration (FFA), in which particles can be energized via elastic reflection and scattering between converging upstream and downstream waves (Jokipii 1966; Fisk 1971; Desai & Giacalone 2016), and shock drift acceleration (SDA), in which charged particles can gain energy through the gradient drift along the induced electric field at the shock surface (Hudson 1965; Decker 1988). Decker (1983) performed a numerical simulation based on single-encounter SDA and showed that the flux of shocked suprathermal particles peaks perpendicular to the magnetic field in the downstream while along the magnetic field in the upstream.

Many studies have been dedicated to the spectral evolution of suprathermal H^+ at energies from above thermal to ~ 50 keV at interplanetary shocks (Frank 1970; Gosling et al. 1981). Using the *Solar Terrestrial Relations Observatory Ahead* spacecraft (*STEREO A*)/Plasma and Suprathermal Ion

Composition instrument (PLASTIC) measurements at 1 au, Yu et al. (2018) selected 12 stream interaction region (SIR) events from 2007 through 2013 according to the SIR list by Jian et al. (2006, 2019) with four criteria: (a) an SIR event with clear, typical structure; (b) existence of a clear reverse shock; (c) a suprathermal H^+ count rate exceeding five per hour in the undisturbed fast solar wind; (d) no contamination of H^+ by He^{2+} particles. They reported that the downstream H^+ at $\sim 10\text{--}80$ keV appears to have a single power-law spectrum in all the events, while the upstream H^+ spectrum appears to have a clear turnover at energies below 35 keV in half of the events, which is consistent with other observations by Fisk & Gloeckler (2012) and Lario et al. (2019). However, the pitch-angle distribution (PAD) of H^+ at these energies has not been well studied. Previously the PAD of ions (without differentiating species) at these energies has been reported to be a field-aligned beam upstream of the shock (e.g., Gosling et al. 1984; Lario et al. 2019) and nearly isotropic in the downstream (Kajdič et al. 2017). At energies around 1 MeV, the PAD of H^+ is reported to be field-aligned in the upstream and field-perpendicular in the downstream (e.g., Pesses et al. 1979, 1984; Tsurutani et al. 1982).

For He^{2+} at the low suprathermal energies, Yu et al. (2017) reported power-law spectra in the downstream region and turnover spectra at energies between ~ 10 and 40 keV/nuc in the upstream region of reverse SIR shocks, with combined measurements from the *Solar and Heliospheric Observatory/Charge, Element, and Isotope Analysis System/Suprathermal Time-Of-Flight (SOHO/CELIAS/STOF)* and the *Advanced Composition Explorer/Solar Wind Ion Composition Spectrometer (ACE/SWICS)*. The PAD of these low-energy

suprathermal He^{2+} is unknown. However, using the measurements from EPACT/STEP on board the *Wind* spacecraft, Ebert et al. (2012) reported an antisunward flow of $\sim 60\text{--}950$ keV/nuc $\text{He}^{2+} > 4$ hr before the arrival, which is downstream of a reverse SIR shock, and a sunward flow after the shock arrival in the upstream region.

The pickup He^+ constitutes an important part of nonthermal He^+ in interplanetary space, which is formed when interstellar neutral He gets ionized and captured by the interplanetary magnetic field (IMF; e.g., Möbius et al. 1985). The velocity distribution function of pickup ions directly after the pickup process generally resembles a torus (e.g., see Figure 1 of Drews et al. 2015) and its maximum velocity typically varies between 0.8 and 1.2 times the solar wind bulk speed in the solar wind frame (Taut et al. 2018). Combining Ulysses SWICS and HISCALE measurements, Gloeckler et al. (2005) reported that He^+ particles downstream of a reverse SIR shock show a flat spectrum at $v/v_{\text{sw}} \lesssim 2$ in the spacecraft frame and a power-law spectrum at $2 < v/v_{\text{sw}} < 10$. Again the angular distribution of He^+ has not been analyzed.

In this work, we present a reverse SIR shock case to study the PADs of H^+ , He^{2+} , and He^+ at suprathermal energies of $\sim 10\text{--}40$ keV/nuc ($\sim 8\text{--}20$ keV/nuc for He^+) for the first time, which is made possible by using the measurements with PLASTIC on board *STEREO A*. We discuss the possible formation of the observed PADs and their implications on the acceleration mechanism of these low-energy suprathermal particles at interplanetary shocks.

2. Instrumentation

The twin *STEREO* spacecraft were launched on 2006 October 25 into heliocentric orbits in the ecliptic plane, one slightly closer than Earth's orbit by less than 0.06 au, the other slightly further out than Earth's orbit by less than 0.1 au. These small orbital differences enabled *STEREO A (B)* to orbit the Sun ahead (behind) of Earth with a longitudinal separation from Earth increasing by about 22° per year (Kaiser et al. 2008). The PLASTIC instrument (Galvin et al. 2008) on board the *STEREO A* spacecraft is a time-of-flight mass spectrometer. It uses a stepped electrostatic analyzer (ESA) system (128 steps from 0.3 to 80 keV e^{-1} in ~ 1 minute) together with a time-of-flight and solid-state detector system to uniquely determine the mass, charge, and energy of an incident ion (see details in Galvin et al. 2008). The ion data in this work are collected with the Solar Wind Section (SWS) of PLASTIC, the entrance of which is centered on the Sun–spacecraft line. The SWS has two entrance apertures: in every ESA cycle, its entrance system can be switched from a main channel to a small channel autonomously with a smaller ($\sim 0.1\%$) geometry factor when the count rate reaches a certain threshold. This special design allows PLASTIC to measure the bulk solar wind as well as its suprathermal tail with comparable counting statistics. For this study, the relevant data are taken from the main channel only. Moreover, the SWS measures the incident angles of particles in an angular acceptance range of $\pm 22.5^\circ$ in and $\pm 20^\circ$ out of the ecliptic plane around the Sun–spacecraft line. It uses an electrostatic deflection system to determine out-of-ecliptic angles with 32 linearly spaced deflection steps and a resistive anode to distinguish in-ecliptic angles of incident particles with 32 linearly spaced position bins. We note that the angular measurements with the small channel are uncertain, so only measurements from the main channel are used to study angular

distributions. In addition, the IMF vector is measured at 8 Hz by the MAGnetometer (MAG) of the In situ Measurements of Particles and CME Transients suite (Luhmann et al. 2008).

In this Letter, we use the pulse height analysis (PHA) data from PLASTIC/SWS, which provide the most detailed information for each incident ion (Galvin et al. 2008; Drews 2013). We extract ion data for H^+ , He^{2+} , and He^+ with rectangular boxes around the calibrated central positions of these three species on the deposited-energy versus time-of-flight plot for each ESA step (see Figure 2.7 of Drews 2009), using the same method as Drews et al. (2012), Drews (2013), and Yu et al. (2018). For each incident particle, its total energy is obtained from the ESA step and its azimuthal (elevation) angle is calculated from the position (deflection) channel number contained in the PHA event (Opitz 2007; Bochsler et al. 2010). We also use the bulk velocity of solar wind protons \vec{V}_{protons} from the PLASTIC level 2 data product in a resolution of 1 minute from https://stereo-ssc.nascom.nasa.gov/data/ins_data/plastic/level2/Protons/. This data product is derived from a Maxwellian fit to the single “Stop” detector rate, which can be taken as a proxy for the majority species H^+ , and is corrected for background and dead time. We note that this data product is derived from the measurements by the small channel, whose angular measurements are uncertain. Furthermore, we use the 1 s magnetic field data from http://aten.igpp.ucla.edu/forms/stereo/heliocentric_level1_magnetic_field.html.

3. Pitch-angle Distributions

The pitch angle (PA) of a charged particle is the angle between the particle's velocity vector and the local magnetic field. As the solar magnetic field is convected outward with the solar wind, the correct frame of reference for the PADs would be moving at the convection speed of the magnetic field. Nemecek et al. (2019) found that this speed is not necessarily the speed of the solar wind protons but rather the DeHoffman–Teller velocity that is shifted by roughly half the Alfvén speed along the direction of the magnetic field (also see Berger et al. 2011). In this frame, the induced electric field vanishes. However, in order to calculate the DeHoffman–Teller velocity, a reliable three-dimensional measurement is required. Because the three-dimensional \vec{V}_{protons} is measured by the small channel of the SWS, the directional information is not reliable. Thus we choose to use the radial component $(\vec{V}_{\text{protons}} \cdot \hat{r}) \hat{r}$ as an estimate of the velocity of the solar wind frame. We estimate the uncertainty of the resulting suprathermal ion velocity in the solar wind frame, $|\vec{V}_{\text{sw}}^{\text{ion}}|$, based on the ratio of half the Alfvén speed, or roughly the velocity difference between the solar wind frame and the DeHoffman–Teller frame, to $|\vec{V}_{\text{sw}}^{\text{ion}}|$, which is $\lesssim 5\%$ for suprathermal ions with $|\vec{V}_{\text{sw}}^{\text{ion}}| > 1.2 \times |(\vec{V}_{\text{protons}} \cdot \hat{r}) \hat{r}|$. The reverse shock case in this study, with an Alfvén speed of ~ 80 km s^{-1} and a solar wind proton speed of ~ 600 km s^{-1} in the vicinity of the shock, is an illustrative example. Furthermore, we use the normalized velocity in the solar wind frame

$$\vec{w}_{\text{sw}} = \frac{\vec{V}_{\text{sw}}^{\text{ion}}}{|(\vec{V}_{\text{protons}} \cdot \hat{r}) \hat{r}|} \quad (\text{and } w_{\text{sw}} = |\vec{w}_{\text{sw}}| \text{ for simplification herein})$$

instead of $\vec{V}_{\text{sw}}^{\text{ion}}$ in the following analysis. We note that the spacecraft aberration has been taken into account and corrected in the above velocities. Figures 1(a)–(b) show the distributions of He^{2+} PHA events in the instrumental frame, accumulated by the main channel of the SWS in a ~ 10 minutes time interval as

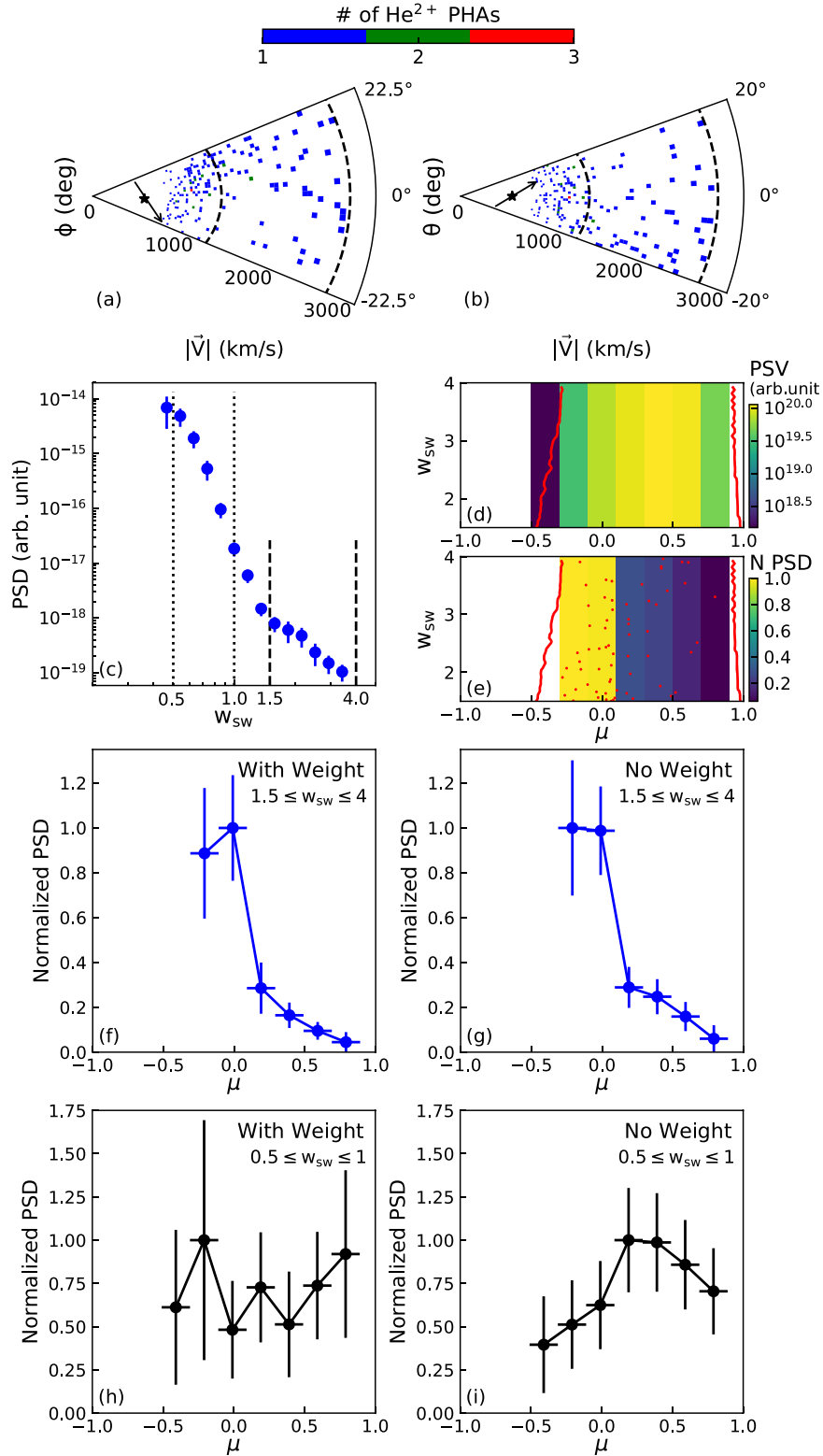


Figure 1. Distributions of He²⁺ PHA events in (a) and out of (b) the ecliptic plane, accumulated by the main channel of the SWS in a ~ 10 minute time interval as an example for illustration. The star marks the average bulk velocity of solar wind protons, and the arrow indicates the average direction of magnetic field during this interval. (c) Average velocity distribution function of He²⁺ in this interval. The dotted lines indicate where $w_{sw} = 0.5$ and $w_{sw} = 1$, and the dashed lines in (a)–(c) indicate where $w_{sw} = 1.5$ and $w_{sw} = 4$. (d) Total PSV covered by all the combinations of ESA step, deflection step, and position bin that fall in each PA bin. (e) PSD in each PA bin, normalized to its maximum among all PA bins. The red contour lines in (d)–(e) indicate the PA coverage and the red dots in (e) represent the transmitted PHA events during this ~ 10 minute interval. (f)–(g) Average PSD at $1.5 \leq w_{sw} \leq 4$ as a function of PA, normalized to its maximum among all PA bins and shown as a line plot with estimated statistical errors. The PSDs are obtained with applying the base rate weight in (d) and without in (e). (h)–(i) Similar to (f)–(g), but for $0.5 \leq w_{sw} \leq 1$. Note that the data shown in this figure are the same data as in the downstream interval “D1” shown in Figure 3.

an example for illustration. Figure 1(c) shows the average spectrum of He^{2+} in the solar wind frame during this example interval. The power-law spectrum at $1.5 \leq w_{\text{sw}} \leq 4$ indicates a strongly accelerated population and particles in this velocity range are likely to have the similar PAD.

Then we use the magnetic field to calculate the cosine of the PA in the solar wind frame according to $\mu = \frac{\vec{w}_{\text{sw}} \cdot \vec{B}}{|\vec{w}_{\text{sw}}| |\vec{B}|}$. The

IMF carries a lot of fluctuations, where \vec{B} changes even on timescales comparable to the gyroperiod of ions. However, we are interested in PADs of particles, not the PA at specific gyro-phases. Therefore, we can ignore changes in \vec{B} faster than the gyroperiod and average \vec{B} for each ion species over its individual gyroperiod. For each PHA event, \vec{B} is averaged in this way centered on its time of measurement, which is defined by the instrumental ESA step. In this way, the nominal μ and w_{sw} , as well as the corresponding phase space volume (PSV), for each instrumental bin, i.e., each combination of ESA step, position bin, and deflection step, can be determined. Then we integrate the number of PHA events (red points in Figure 1(e)) and the PSV (see Figure 1(d)) over ranges in μ and w_{sw} . The ratio of both is proportional to the phase space density (PSD, no efficiencies have been applied) for the selected ranges in μ and w_{sw} . For this example, we set up six wide linearly spaced bins at $-0.3 \leq \mu \leq 0.9$ according to the PA coverage and a whole bin at $1.5 \leq w_{\text{sw}} \leq 4$ according to the power-law spectrum. Then we obtain the PAD as well as the normalized PAD by normalizing it to the maximum among all PA bins. The normalized PAD is shown as a color plot in Figure 1(e) as well as a line plot with statistical errors in Figure 1(g). The coverage in μ is widened by the fluctuations of the magnetic field direction within the 10 minutes integration time. Only the PA bin with reasonable coverage is taken into account, i.e., the PA bins with a PSV larger than one-tenth the maximum PSV among all PA bins and good coverage for all w_{sw} in the selected range. In addition, the velocity difference between the solar wind frame and the DeHoffman–Teller frame of roughly half the Alfvén speed along the magnetic field causes a maximum error of ~ 0.05 in μ for ions with $|\mu| \sim 0$, but no error for $|\mu| \sim 1$. Also, this error does not significantly influence the binning in μ for the large PA bin width of 0.2.

An issue with PLASTIC PHA data is that due to the limited telemetry, only a certain number of PHA events per minute that are randomly selected on board the spacecraft can be transmitted to Earth (see more details in Galvin et al. 2008). So the PHA words that are transmitted are only a sample from all the onboard measured events, whose total number is also transmitted. The idea behind it is that each PHA word can be weighted by the ratio of the total number of measured events N_{events} and the number of selected PHA words N_{PHA} , so-called base rate weights (e.g., Drews 2013). This approach is fine as long as the transmitted PHA words resemble the underlying distributions. In cases of low particle flux (e.g., suprathermal particles, heavy ions), the base rate weight is close to 1, and no correction of the PHA distributions is needed. These cases typically require long integration times to get enough counting statistics. By applying the base rate weight, we are able to normalize PHA event rates and determine the particle flux for each combination of ESA step and deflection step also for higher ion fluxes. However, full correction of the three-dimensional combination, including the position bin, is not possible, because count rate data separate for each position bin

needed for normalization are unavailable. This means that the one-dimensional E/q spectra could be well recovered, while the recovery of three-dimensional distribution or PAD might be biased and thus has to be taken with a grain of salt.

Figure 1(f) shows the normalized PAD of He^{2+} at $1.5 \leq w_{\text{sw}} \leq 4$ to which we have applied the base rate weight for each PHA event. Compared to the normalized PAD without applying the base rate weight shown in Figure 1(g), it can be seen that the qualitative results do not change. We take this as confirmation that the onboard random selection of PHAs due to limited telemetry does not substantially influence our results. Thus the randomly selected PHA events represent the original population qualitatively correctly within statistical uncertainties, for He^{2+} at $1.5 \leq w_{\text{sw}} \leq 4$. On the other hand, Figures 1(h) and (i) show the weighted and unweighted normalized PADs, respectively, for He^{2+} at $0.5 \leq w_{\text{sw}} \leq 1$, where the base rate weight is high (~ 10 – 100). It appears that the weighted normalized PAD differs significantly from the unweighted normalized PAD, which indicates that the PHA events of He^{2+} at $0.5 \leq w_{\text{sw}} \leq 1$ may not represent the underlying distribution well. For these PHA events with high weights (~ 10 – 100), one has to be very careful when analyzing their three-dimensional distributions and thus we only focus on PHA events with relatively low base rate weights, like He^{2+} at $w_{\text{sw}} \geq 1.5$.

4. Reverse Shock of an SIR

Interplanetary reverse shocks are usually observed at the trailing edges of SIRs due to the steepening of reverse waves (e.g., Hundhausen & Gosling 1976). It is suspected that particles accelerated at the shock could be transported to the downstream region along the magnetic field, which is generally in the antisunward direction for reverse shocks. Thus a reverse SIR shock would provide an opportunity to directly observe the escaping particles from the shock to its downstream region with the sunward-looking SWS and examine the PADs of shocked particles in the downstream region. To study the PADs in the direct vicinity of a shock, we need good counting statistics to get reliable PADs. Good statistics must be obtained for individual magnetic flux tubes, because the PADs are not necessarily constant across different regimes. In addition, it would be favorable to have some smooth rotations of the magnetic field inside the flux tubes to get a better PA coverage. Yu et al. (2018) analyzed PLASTIC data to study the large-scale spectral evolution of H^+ downstream of 12 reverse SIR shocks. For our study, we select the 2008 March 9 shock as a candidate, which has the best combination of counting statistics and magnetic field variability.

Figure 2 shows a timeline of the candidate reverse shock observed by *STEREO A* at ~ 1950 UT on 2008 March 9 (indicated by the right blue line), which is the trailing edge of an SIR event (see Figure 3 of Yu et al. 2018). This shock is identified by Jian et al. (2019) to be a quasi-perpendicular shock with an angle between the shock normal and the upstream IMF of $79^\circ.4$. It has a magnetosonic Mach number of 1.44, magnetic compression ratio of 1.59, and density compression ratio of 1.83. We identify four magnetic flux tubes bounded by dramatic magnetic field changes, either in magnitude or directions (indicated by the vertical dashed lines). We mark the ~ 5 minute upstream interval adjacent to the shock as “U1,” the ~ 10 minute interval further upstream as “U2,” the ~ 10 minute downstream interval adjacent to the shock as “D1,” and the ~ 20 minute interval further downstream as “D2” (measurements within the

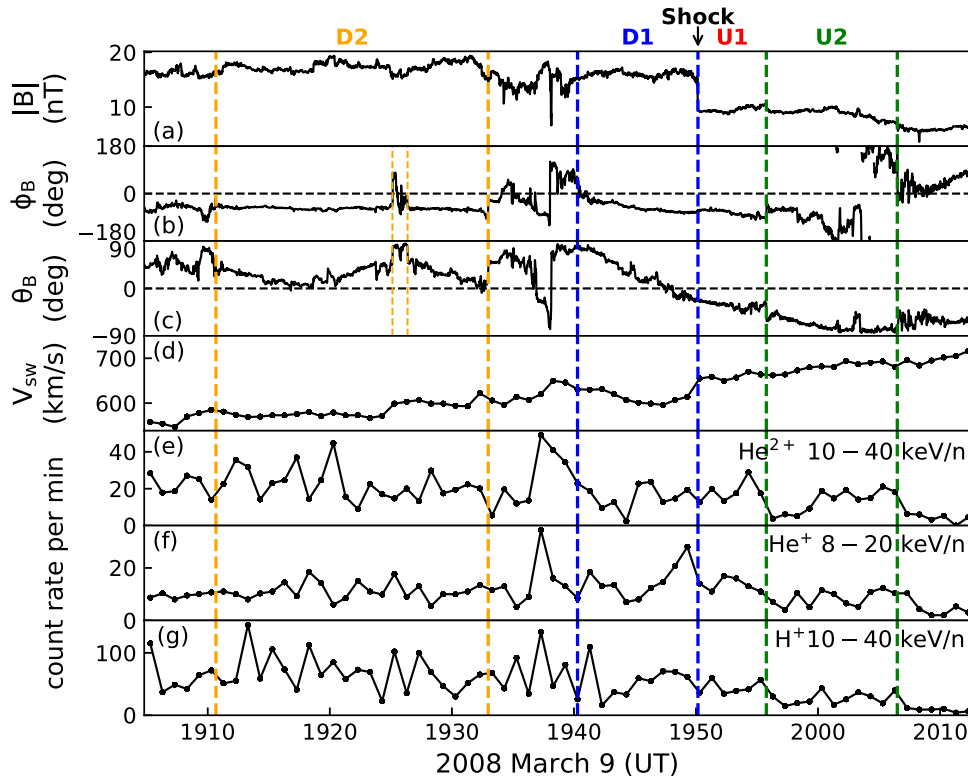


Figure 2. Summary plot of the reverse SIR shock on 2008 March 9. (a)–(c) Magnitude $|B|$, azimuthal angle ϕ_B , and elevation angle θ_B of IMF in 1 s resolution, (d) solar wind proton bulk velocity in 1 minute resolution. (e)–(g) Count rate per minute of ~ 10 – 40 keV/nuc He^{2+} , ~ 8 – 20 keV/nuc He^+ , and ~ 10 – 40 keV/nuc H^+ . The right blue line indicates the shock arrival at ~ 1950 UT, and the bold colored lines mark the boundaries of the four periods analyzed in this study.

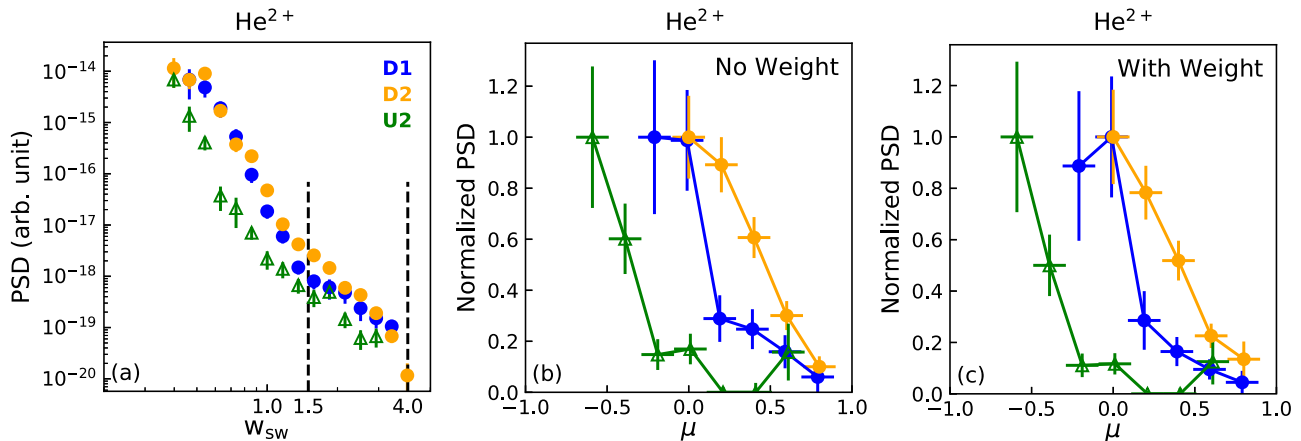


Figure 3. (a) Average velocity distribution functions of He^{2+} observed by the SWS during “D1,” “D2,” and “U2” indicated in Figure 2. (b)–(c) PSD averaged over $w_{\text{sw}} \sim 1.5$ – 4 (dashed lines in (a)) as a function of PA, normalized to its maximum among all PA bins, shown as a line plot with estimated statistical errors for the three time periods. The PSDs are obtained with applying the base rate weight in (c) and without in (b).

1 minute substructure marked out by the thin vertical lines in panels (b)–(c) are removed in the analysis). Suprathermal ions measured in the downstream intervals likely reflect shocked ions. In the following, we present the velocity and PADs of He^{2+} , He^+ , and H^+ for the three time periods “D2,” “D1,” and “U2,” in which the high count rates of all species over an extended time interval under smoothly rotating magnetic field produce reliable PADs over a wide range of PAs. Then we present the distributions for “U1,” which is the region directly upstream of the shock, in comparison with the distributions for “U2” further upstream.

Figure 3(a) shows the average He^{2+} spectra in the solar wind frame for the three periods, after applying the base rate weight,

followed by the respective normalized PADs with no weights applied in Figure 3(b) and with weights in Figure 3(c). How the velocity and PADs have been obtained from the original PHA events has been demonstrated in detail for the example of the 10 minute interval “D1” in Figure 1. Using the same method as for “D1,” we obtain the velocity distributions and normalized PADs for intervals “D2” and “U2,” shown in orange and green, respectively.

We find that the He^{2+} spectra can be fitted with a single power law at $w_{\text{sw}} \sim 1$ – 4 both downstream and upstream, consistent with the observation by Yu et al. (2017). Then we select a wide w_{sw} bin from 1.5 to 4 as a compromise between improving counting statistics and minimizing bias caused by

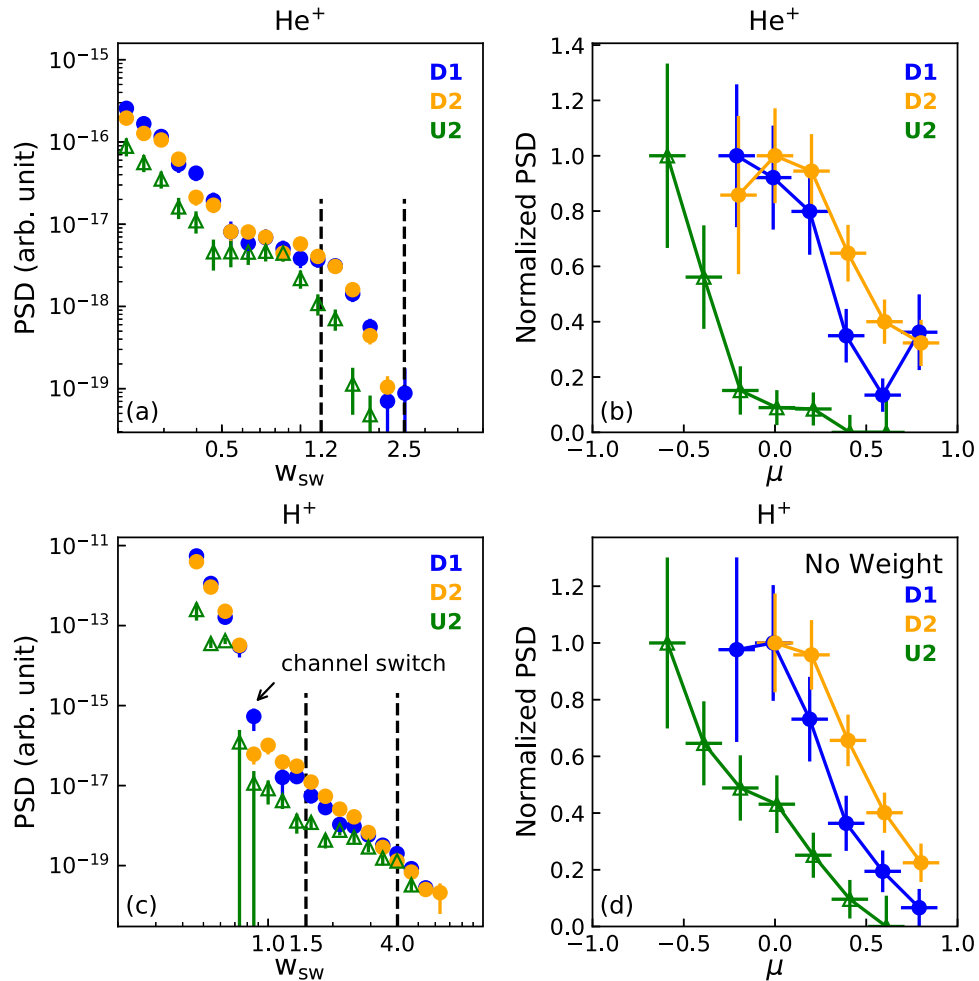


Figure 4. (a)–(b) Average velocity distribution functions and normalized PADs (normalized to the maximum among all PA bins) of He⁺ observed by the SWS during “D1,” “D2,” and “U2” indicated in Figure 2; (c)–(d) same as (a)–(b), but for H⁺. The PADs are averaged over $w_{sw} \sim 1.2$ –2.5 (dashed lines in (a)) for He⁺ and $w_{sw} \sim 1.5$ –4 (dashed lines in (c)) for H⁺. The selected range of $w_{sw} \sim 1.5$ –4 in (c) is far above the velocity of the small channel switch. The PSDs in (d) are obtained without applying the base rate weight. The estimated statistical errors are shown in each panel.

incomplete transmission of PHA events. For He²⁺ at $w_{sw} \sim 1.5$ –4, the randomly selected and transmitted PHA events generally take up $\sim 70\%$ of all the measured PHA events on board the spacecraft.

Furthermore, we find that in both downstream periods, “D1” and “D2,” the PAD of He²⁺ shows significantly higher intensity in the direction perpendicular to the IMF than in the parallel direction. This is interesting because particles accelerated at this reverse shock are expected to escape into the downstream region parallel to the magnetic field. In this case where the downstream magnetic field is generally pointing antisunward ($-90^\circ < B_\phi < 90^\circ$ in Figure 2(b)), this would be for $\mu > 0$. However, the downstream PAD at $\mu < -0.3$ is not or not well measured by the SWS due to the magnetic field configuration, and we cannot rule out that there is an unobserved beam in the antiparallel direction. But the existence of a beam traveling from far downstream toward the shock front is very unlikely, especially given the fact that no interplanetary coronal mass ejection (ICME) is observed within 3 days before this reverse shock (Jian et al. 2018).

For the upstream period “U2,” the PAD shows a clear beam at $\mu < 0$, which is due to the escaping particles along the upstream magnetic field, which points antisunward at the beginning and then turns smoothly out-of-ecliptic (see

Figures 2(b)–(c)). This special magnetic configuration provides an opportunity to measure particles that escape from the shock to its upstream region with the SWS. However, this observed beam could originate from a part of the shock that is far south of the ecliptic plane and travel along the bending magnetic field to reach the spacecraft in the ecliptic plane, rather than from the part of the shock observed by the spacecraft.

Figure 3(c) shows the normalized PADs of He²⁺ in the three time periods to which we have applied the base rate weight for each PHA event, although it might lead to biased PADs to some extent. Compared to the normalized PADs without applying the base rate weight shown in Figure 3(b), it can be seen that the qualitative results do not change, i.e., the PAD shows the perpendicular anisotropy downstream of the shock and an antiparallel beam upstream. Again this confirms that the randomly selected PHA events represent the original population qualitatively correctly within statistical uncertainties.

After normalization by the base rate weight, the He⁺ spectra in the solar wind frame (Figure 4(a)) show the signature of power-law spectra at $w_{sw} \sim 1.2$ –2.5 (inconclusive due to the narrow velocity interval), consistent with the observation by Gloeckler et al. (2005). It also exceeds the usual cutoff velocity of $w_{sw} \sim 0.8$ –1.2 for the common pickup He⁺ (Taut et al. 2018). For He⁺ at $w_{sw} \sim 1.2$ –2.5, the base rate weight for each

PHA event is always 1, indicating that all the PHA events measured on board the spacecraft are transmitted to Earth due to the low flux of He^+ along with its high priority assigned by the onboard probability selection mechanism (Galvin et al. 2008). Thus the PADs of He^+ shown in Figure 4(b) are unbiased by the onboard selection scheme. Again, we find that in the downstream, the PSD is significantly higher in the perpendicular direction than in the parallel direction (the escape direction into the downstream region), while upstream, the PAD shows a clear beam antiparallel to the IMF (the escape direction into the upstream region).

Figure 4(c) shows the spectra of H^+ in the solar wind frame after normalization by the base rate weight, combining the measurements in the main channel and small channel. The downstream spectra can be characterized by a single power law at $w_{\text{sw}} \sim 1-5$, consistent with previous observations (e.g., Yu et al. 2018; Lario et al. 2019). We select the H^+ PHA events in the range of $w_{\text{sw}} \sim 1.5-4$, the same range as for He^{2+} , to obtain the normalized PAD shown in Figure 4(d), without applying the base rate weight, since we have demonstrated above that the randomly selected PHA events represent the original population qualitatively correctly. Similar to He^{2+} and He^+ , the downstream PSD of H^+ is significantly higher perpendicular to the IMF than in the parallel direction, and the upstream PAD shows a clear beam antiparallel to the IMF, although with a large angular width. We note that the PADs of H^+ with normalization by base rate weight (not shown) qualitatively show the same results as shown in Figure 4(c), though the transmitted H^+ PHA events at $w_{\text{sw}} \sim 1.5-4$ take up only $\sim 20\%$ of all the measured PHA events on board the spacecraft.

In Figures 5(a)–(c) we compare the normalized PADs of He^{2+} , He^+ , and H^+ for each time period. During the downstream intervals “D1” and “D2,” these three species show very similar PADs, significantly higher PSD perpendicular to the IMF than parallel. During the upstream interval “U2,” the PADs of all three species show a clear beam in the antiparallel direction, but the angular width of the H^+ beam appears to be larger than the He^{2+} and He^+ beams.

Figures 5(d)–(f) show a comparison of the PADs observed during the upstream intervals “U1” and “U2,” which are both normalized to the maximum PSD observed in “U2,” for all three species. For He^{2+} , the PAD in “U1” shows a wide bump at $\mu \sim -0.3-0.5$, which is different from the PAD of a clear beam in “U2.” Because of the limited PA coverage in “U1,” it is uncertain whether there is a beam antiparallel to the IMF or not. For He^+ , the PAD in “U1” appears to show a double-peak structure, a main beam at $\mu \sim -0.3$, and an additional bump at $\mu \sim 0.3$, different from the PAD of a clear beam in “U2.” On the other hand for H^+ , the PADs in “U1” and “U2” show a similar clear beam in the antiparallel direction (red dashed line and green solid line). Furthermore, the PSDs of all three species are generally higher in “U1” than in “U2,” because “U1” is closer to the shock.

5. Summary and Discussion

We examined the PADs of suprathermal H^+ , He^{2+} , and He^+ at $w_{\text{sw}} \sim 1.5-4$ in close proximity downstream and upstream of the 2008 March 9 reverse shock observed by *STEREO A*/PLASTIC. We find that both downstream and upstream close to the shock, the shocked suprathermal particles of three species all appear to have a power-law-like spectrum at

$w_{\text{sw}} \sim 1.5-4$ ($\sim 1.2-2.5$ for He^+ ; see Figures 3 and 4). The PADs of these three species also show very similar behavior near the shock (Figures 5(a)–(c)): in the downstream region, the PSD is significantly higher in the direction perpendicular to the IMF than in the parallel direction, along which accelerated particles at the shock front may escape into the downstream region; in the upstream region, the PAD shows a clear beam antiparallel to the IMF, i.e., the direction along which accelerated particles at the shock would escape into the upstream region. In addition, we find a double-peak structure, a beam antiparallel to the IMF with an additional bump in the opposite direction, in the PAD of suprathermal He^+ observed in the upstream region very close to the shock.

The very similar behavior of H^+ , He^{2+} , and He^+ PADs near the shock could indicate shock acceleration by the same mechanism, e.g., SDA, which works nearly the same for all positively charged particles. In the downstream region of the shock, we find that the PSD of suprathermal ions is significantly higher in the direction perpendicular to the IMF compared to the parallel direction (Figures 5(a)–(b)). This observation could indicate that particles are more efficiently accelerated perpendicular to the IMF at the shock. Then the field-perpendicular particles would travel with the solar wind or the frozen-in magnetic field downstream, maintaining the field-perpendicular PAD. Such more efficient acceleration perpendicular to the IMF is favored by both the SDA theory and single-encounter SDA simulations (Decker 1983), as particles would gain the perpendicular energy when drifting along the induced electric field. Furthermore, particles traveling perpendicular to the IMF also have the largest gradient drift velocity. This has also been supported by the observation of field-perpendicular PADs of $\sim 0.6-3.4$ MeV protons at SIR shocks by Pesses et al. (1979) and the observation of the more efficient acceleration in the direction perpendicular to IMF of 1 MeV ions at ICME-driven shocks by Yang et al. (2018, 2019). Such downstream field-perpendicular PADs at energies from ~ 10 keV to several MeV are inconsistent with the formation of isotropic PADs by FFA (e.g., Drury 1983; Giacalone 2015).

Ebert et al. (2012) presented a reverse SIR shock case where a beam of $\sim 60-950$ keV/nuc He^{2+} traveling away from the shock was observed ~ 4 hr before the shock arrival. On the other hand, our study suggests that He^{2+} at lower energies of $\sim 10-40$ keV/nuc show a field-perpendicular PAD in the ~ 40 minute downstream interval adjacent to the shock. Such different observations could be explained by the possibility that the PAD of suprathermal He^{2+} is field-perpendicular in the downstream interval of several hours adjacent to the shock. In the more distant downstream region, e.g., >4 hr away from the shock, possibly due to a switch into different magnetic flux tubes, the PAD transitions to a beam traveling away from the shock.

In the upstream PADs, H^+ , He^{2+} , and He^+ show a clear beam due to escaping particles from the shock (Figure 5(c)), which is consistent with the previous observations of ~ 10 keV ions upstream of interplanetary forward shocks by Lario et al. (2019), $\sim 60-950$ keV/nuc He^{2+} upstream of a reverse SIR shock by Ebert et al. (2012), and $\sim 0.6-3.4$ MeV H^+ upstream SIR-associated shocks by Pesses et al. (1979, 1984). However, the escaping beam of H^+ appears to be significantly wider than the He^{2+} and He^+ beam, possibly due to stronger scattering of H^+ than He^{2+} and He^+ , possibly by wave-particle interaction. Furthermore, we note that in the ~ 5 minute upstream interval

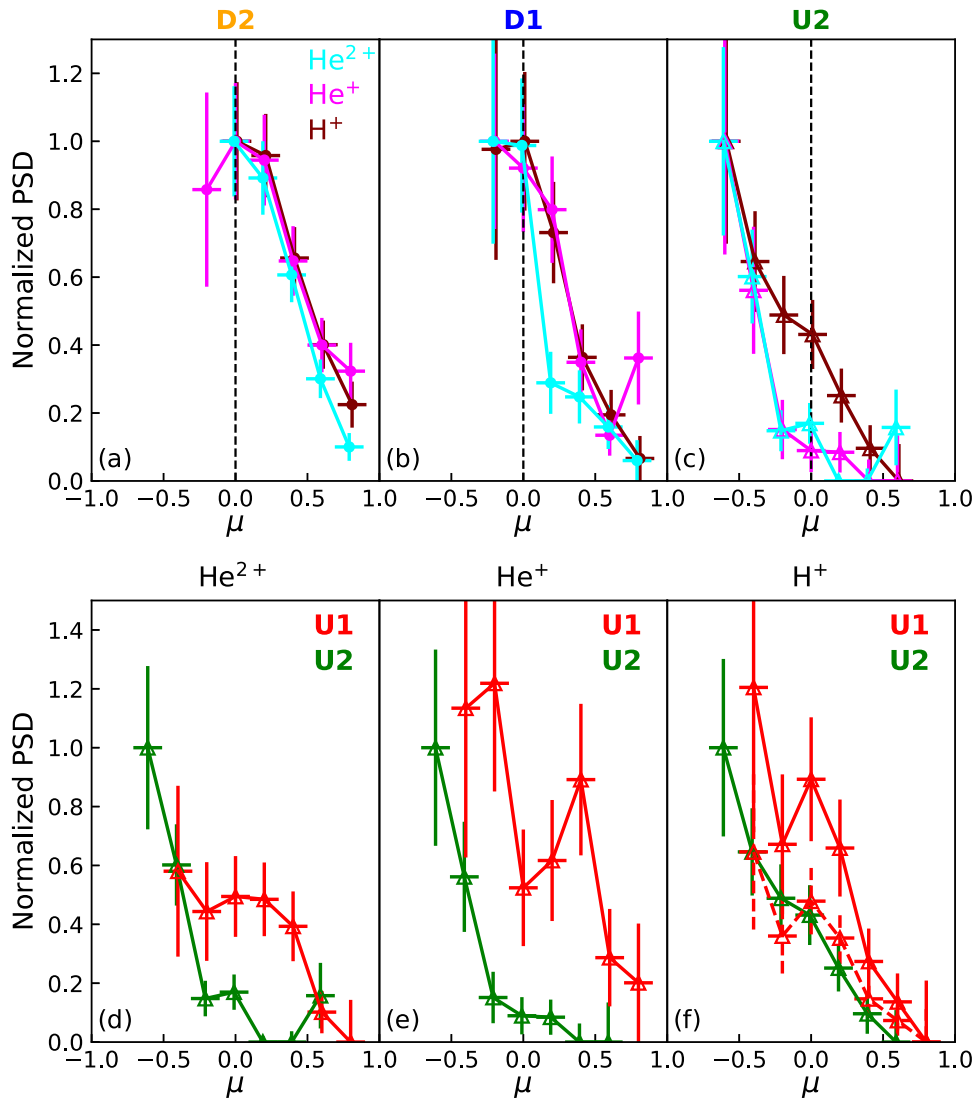


Figure 5. (a)–(c) Normalized PADs of ~ 10 – 40 keV/nuc H^+ , He^{2+} and ~ 8 – 20 keV/nuc He^+ in “D2” (a), “D1” (b), and “U2” (c) indicated in Figure 2. The estimated statistical errors are shown. (d)–(f) Comparison of the PADs observed during the upstream intervals “U1” and “U2” for He^{2+} (d), He^+ (e), and H^+ (f). For each ion species, the PSDs in “U1” and “U2” are both normalized to the maximum PSD observed in “U2,” shown as solid lines. In order to compare the width of the H^+ beam, the PSDs in “U1” are further normalized to the PSD at $-0.5 < \mu < -0.3$ in “U2,” shown as the dashed line in (f). The estimated statistical errors are also shown.

“U1” adjacent to the shock, the magnetic configuration does not provide good conditions for the SWS to fully observe the beam escaping from the shock. The PAD of He^{2+} in “U1” shows a significant bump at $\mu \sim 0$ (Figure 5(d)), different from the PADs observed in “U2,” the upstream interval farther away from the shock. The bump might be due to the superposition of the escaping beam and the field-perpendicular accelerated particles diffusing into the upstream very close to the shock. Furthermore, the PAD of He^+ in “U1” shows a beam antiparallel to the IMF with an additional bump at $\mu \sim 0.3$ (Figure 5(e)), which disappears in “U2.” This intermittent double-peak structure could be evidence for bidirectional beams that are expected upstream very close to the shock, not too far upstream (Erdős & Balogh 1994; Fraschetti & Giacalone 2015). Bidirectional beams could result from the short-lived trapping of suprathermal ions along a field line with both sides connected to the shock.

In this Letter, we presented the PADs of superthermal H^+ , He^{2+} at ~ 10 – 40 keV/nuc and He^+ at ~ 8 – 20 keV/nuc, for the first time, in the vicinity of a reverse SIR shock. In the


downstream region, we find that the ion fluxes of all three species are substantially enhanced perpendicular to the magnetic field over the parallel direction, which is consistent with SDA. Upstream of the shock the ions appear to be streaming away from the shock along the magnetic field, as is typically observed upstream of quasi-perpendicular shocks. A future statistical study of the spectra and/or PADs of low-energy suprathermal ions as well as their variations with shock parameters could help us better understand the in situ acceleration of these ions at interplanetary shocks.

L.Y. is supported by the China Scholarship Council for his one-year stay at CAU. The research at Peking University is supported in part by NSFC under contracts 41861134033, 41774183. L.B. thanks German space agency DLR for support under grant 50 OC 1501. R.W.S. thanks the German space agency DLR for support under grants 50 OT 1201, 50 OT 1501, and 50 OT 1701 and thanks ISSI for its hospitality and support of parts of this work. UNH funding was provided through NASA *STEREO* grant 80NSSC17K0556. E.M. thanks

NASA HSR Grant NNX16AF79G and Heliophysics Grand Challenge Grant 80NSSC17K000 for partial support.

ORCID iDs

Liu Yang  <https://orcid.org/0000-0002-6416-1538>

Robert F. Wimmer-Schweingruber  <https://orcid.org/0000-0002-7388-173X>

Linghua Wang  <https://orcid.org/0000-0001-7309-4325>

Eberhard Möbius  <https://orcid.org/0000-0002-2745-6978>

References

- Asbridge, J., Bame, S., & Strong, I. 1968, *JGR*, **73**, 5777
- Berger, L., Wimmer-Schweingruber, R., & Gloeckler, G. 2011, *PhRvL*, **106**, 151103
- Bochsler, P., Lee, M. A., Karrer, R., et al. 2010, in AIP Conf. Proc. 1216, Twelfth International Solar Wind Conference, ed. M. Maksimovic et al. (Melville, NY: AIP), 257
- Bryant, D. A., Cline, T., Desai, U., & McDonald, F. B. 1962, *JGR*, **67**, 4983
- Decker, R. B. 1983, *JGR*, **88**, 9959
- Decker, R. B. 1988, *SSRv*, **48**, 195
- Desai, M., & Giacalone, J. 2016, *LRSP*, **13**, 3
- Dresing, N., Theesen, S., Klassen, A., & Heber, B. 2016, *A&A*, **588**, A17
- Drews, C. 2009, Diploma thesis, Inst. für Experimentelle und Angewandte Physik der Christian-Albrechts-Univ.
- Drews, C. 2013, PhD thesis, Christian-Albrechts Universität Kiel
- Drews, C., Berger, L., Taut, A., Peleikis, T., & Wimmer-Schweingruber, R. 2015, *A&A*, **575**, A97
- Drews, C., Berger, L., Wimmer-Schweingruber, R. F., et al. 2012, *JGRA*, **117**, A09106
- Drury, L. O. 1983, *RPPh*, **46**, 973
- Ebert, R. W., Desai, M. I., Dayeh, M. A., & Mason, G. M. 2012, *ApJL*, **754**, L30
- Erdős, G., & Balogh, A. 1994, *ApJS*, **90**, 553
- Fisk, L. A. 1971, *JGR*, **76**, 1662
- Fisk, L. A., & Gloeckler, G. 2012, *SSRv*, **173**, 433
- Frank, L. A. 1970, *JGR*, **75**, 707
- Fraschetti, F., & Giacalone, J. 2015, *MNRAS*, **448**, 3555
- Galvin, A. B., Kistler, L. M., Popecki, M. A., et al. 2008, *SSRv*, **136**, 437
- Giacalone, J. 2012, *ApJ*, **761**, 28
- Giacalone, J. 2015, *ApJ*, **799**, 80
- Gloeckler, G., Fisk, L., & Lanzerotti, L. 2005, in Proc. Solar Wind 11/SOHO 16, Connecting Sun and Heliosphere 592, ed. H. Lacoste (Noordwijk: ESA), 107
- Gosling, J. T., Asbridge, J. R., Bame, S. J., et al. 1981, *JGR*, **86**, 547
- Gosling, J. T., Bame, S. J., Feldman, W. C., et al. 1984, *JGR*, **89**, 5409
- Ho, G. C., Lario, D., Decker, R. B., et al. 2003, Proc. ICRC (Tsukuba), **6**, 3689
- Hudson, P. D. 1965, *MNRAS*, **131**, 23
- Hundhausen, A. J., & Gosling, J. T. 1976, *JGR*, **81**, 1436
- Jian, L., Luhmann, J., Russell, C., & Galvin, A. 2019, *SoPh*, **294**, 31
- Jian, L., Russell, C., Luhmann, J., & Galvin, A. 2018, *ApJ*, **855**, 114
- Jian, L., Russell, C., Luhmann, J., & Skoug, R. 2006, *SoPh*, **239**, 337
- Jokipii, J. R. 1966, *ApJ*, **146**, 480
- Kaiser, M. L., Kucera, T., Davila, J., et al. 2008, *SSRv*, **136**, 5
- Kajdič, P., Hietala, H., & Blanco-Cano, X. 2017, *ApJL*, **849**, L27
- Kallenrode, M.-B. 2013, Space Physics: An Introduction to Plasmas and Particles in the Heliosphere and Magnetospheres (3rd ed.; Berlin: Springer)
- Kennel, C., Scarf, F., Coroniti, F., et al. 1984, *JGR*, **89**, 5419
- Lario, D., Berger, L., Decker, R., et al. 2019, *AJ*, **158**, 12
- Luhmann, J. G., Curtis, D. W., Schroeder, P., et al. 2008, *SSRv*, **136**, 117
- Möbius, E., Hovestadt, D., Klecker, B., et al. 1985, *Natur*, **318**, 426
- Nemecek, Z., Durovcova, T., Safrankova, J., et al. 2019, *ApJ*, in press
- Opitz, A. 2007, PhD thesis, Universität Bern
- Pesses, M., Van Allen, J., Tsurutani, B., & Smith, E. 1984, *JGR*, **89**, 37
- Pesses, M. E., Tsurutani, B. T., Van Allen, J. A., & Smith, E. 1979, *JGR*, **84**, 7297
- Qin, G., Kong, F.-J., & Zhang, L.-H. 2018, *ApJ*, **860**, 3
- Taut, A., Berger, L., Möbius, E., et al. 2018, *A&A*, **611**, A61
- Tsurutani, B., & Lin, R. 1985, *JGR*, **90**, 1
- Tsurutani, B., Smith, E., Pyle, K., & Simpson, J. 1982, *JGR*, **87**, 7389
- Yang, L., Wang, L., Li, G., et al. 2018, *ApJ*, **853**, 89
- Yang, L., Wang, L., Li, G., et al. 2019, *ApJ*, **875**, 104
- Yu, J., Berger, L., Drews, C., Wimmer-Schweingruber, R., & Taut, A. 2018, *A&A*, **615**, A126
- Yu, J., Berger, L., Wimmer-Schweingruber, R., et al. 2017, *A&A*, **599**, A13